Months-long crustal deformation driven by aseismic slips and pore pressure transients triggered by local and regional earthquakes

Zhou Lu[1*], Lianxing Wen[2]

[1]Laboratory of Seismology and Physics of Earth's Interior; School of Earth and Space Sciences, University of Science and Technology of China, Hefei, China

[2]Department of Geosciences, State University of New York at Stony Brook, Stony Brook, NY, USA

[*]Corresponding author: Zhou Lu (luzhou@mail.ustc.edu.cn)

Key points:

- We observe strong months-long change of strain and pore pressure after four Mw 4.5+ earthquakes in borehole strainmeters at Anza, California
- The postseismic strains last 40–100 days, and exhibit different trends and larger amplitudes (up to 1e−7) compared to coseismic strains
- Postseismic strains = poroelastic strain by earthquake-induced pore pressure change + elastic strain by an earthquake-triggered aseismic slip

Abstract

Strong strain and pore pressure changes are observed after three Mw 4.5+ local and one Mw 7.2 regional earthquakes during 2010–2017 in borehole strainmeters near Anza, California. The strain change emerges immediately after the earthquakes and lasts 40–100 days with amplitudes up to 10^{-7}, larger than the coseismic strain offsets. The pore pressure exhibits change immediately after the earthquakes at some boreholes and with a delay of 4–10 days at the others. A joint analysis of the observed postseismic strain and pore pressure change suggests that the postseismic strains could be explained by combined effects of poroelastic deformation due to earthquake-induced pore pressure change and elastic deformation due to an earthquake-triggered aseismic slip on a nearby fault. Our study indicates that, in addition to possible aseismic fault slips triggered by an earthquake, pore pressure changes after the earthquake could be even more important in producing postseismic deformation.

Plain language summary

Understanding the physical mechanisms producing postseismic deformation is important for assessing fault slip budget and seismic hazards. In this study, we seek to clarify possible roles of aseismic slip and pore pressure change in producing postseismic deformation through a joint analysis of postseismic strains and pore pressure change observed following four Mw 4.5+ earthquakes in southern California. The postseismic strains start immediately after the earthquakes and last 40–100 days. They also exhibit larger amplitudes and different relative amplitudes among different strain components compared to the coseismic strain offsets. The pore pressure exhibits postseismic changes immediately after the earthquakes in some boreholes and with a delay of 4–10 days at the others. These observations are well explained by a mechanism that the mainshock earthquake instantly triggers an aseismic slip in a neighboring fault and alters the hydrological conditions in the region; the change of hydrological condition results in postseismic pore pressure changes and produces poroelastic deformation in the region, while the aseismic slip produces elastic deformation. This study indicates that, in addition to possible aseismic fault slips triggered by an earthquake, pore pressure changes after the earthquake could play an even more important role in producing postseismic deformation.

1. Introduction

Understanding postseismic deformation is important for assessing seismic hazards as the deformation changes fault slip budget and stress state in seismogenic zones (Gualandi et al., 2020; Iinuma et al., 2016; Johanson et al., 2006; Xu et al., 2020). Postseismic deformation can be induced by many physical mechanisms and is useful for constraining many physical properties of the Earth. For example, postseismic deformation induced by an aseismic slip is useful for constraining fault frictional properties (Johnson et al., 2006), while that related to viscoelastic relaxation of the coseismic deformation is routinely used to infer rheological properties of the lower crust and upper mantle (Hu et al., 2016; Jónsson, 2008; Nur & Mavko, 1974). Additionally, postseismic deformation produced by pore fluid flow can also be used to constrain near surface hydrological properties (Jónsson et al., 2003; Peltzer et al., 1998).

Postseismic deformation produced by aseismic slip has attracted close attentions from various studies. For example, such deformation has been observed in the nature by many instruments, including theodolite (Scholz et al., 1969; Smith & Wyss, 1968), GPS (Johnson et al., 2006; Yu et al., 2003), InSAR (Johanson et al., 2006), strainmeter (Alwahedi & Hawthorne, 2019; Hawthorne et al., 2016; Inbal et al., 2017), and sea floor geodetic observation (Iinuma et al., 2016). Additionally, postseismic aseismic slip has also been generated in numerical simulations (Helmstetter & Shaw, 2009).

By contrast, postseismic deformation produced by pore fluid has been reported by only

a few studies (e.g., Hughes et al., 2010; Jónsson et al., 2003; Peltzer et al., 1998). However, such fluid-related postseismic deformation is likely significant in the crust, as some earthquakes have been reported to induce significant changes in hydrological conditions (Manga & Wang, 2007; Matsumoto et al., 2003; Roeloffs, 1998; C.-Y. Wang et al., 2004) and crustal deformation related to hydrological process has been observed to be significant (Fu & Freymueller, 2012; Lu & Wen, 2018; Silverii et al., 2019; C.-Y. Wang & Barbour, 2017; Zhan et al., 2017).

Distinguishing between postseismic pore fluid and aseismic slip from field observations and understanding the role of each mechanism in producing postseismic deformation are critical for inferring the related geophysical processes and properties of the Earth, as these two processes have been reported to be closely related after some earthquakes. For example, both theoretical analysis and numerical modeling have shown that pore fluid flow after an earthquake plays an important role in fault slip (Byerlee, 1993; Sibson, 1992), and fluid pressure change following the 2016 Kaikōura, New Zealand earthquake has also been inferred to drive aseismic fault slip (Hamling & Upton, 2018). So far, many previous studies have considered separately the roles of postseismic pore fluid and aseismic slip in explaining postseismic deformations (e.g., Alwahedi & Hawthorne, 2019; Inbal et al., 2017; Jónsson et al., 2003; Peltzer et al., 1998) or have combined the two processes for only large earthquakes (c.f., Mw>6) (Kang Wang & Fialko, 2018). Few studies combine these two processes to explore their interplay in explaining some of the postseismic deformations, although these two processes have

been reported to be closely related as discussed above.

In this study, we seek to clarify possible roles of aseismic slip and pore pressure change in producing postseismic deformation through a joint analysis of postseismic strains and pore pressure change observed following four Mw 4.5+ earthquakes in southern California. We report the observation of strong postseismic changes of strain and pore pressure in section 2, and discuss possible physical mechanisms in section 3.

2. Observation of strong postseismic changes of strain and pore pressure

We use the strain data recorded in the Network of the Americas (NOTA) borehole strainmeters and the pore pressure data recorded in the strainmeter boreholes to study postseismic deformation (Figure 1a). The NOTA strainmeters are placed in boreholes at depths of 120–250 m along the plate boundary zones of the western United States and on Vancouver Island of Canada (Silver & PBO Steering Committee, 2000). Each strainmeter consists of four horizontal gauges that measure elongation of the surrounding rock at different directions with a resolution of about 10^{-10} (Gladwin, 1984). Those gauge measurements could be converted into a horizontal strain tensor through calibration matrixes obtained based on tidal response (Hodgkinson et al., 2013; Roeloffs, 2010). Auxiliary data are also measured at the strainmeter sites, including barometric pressure and rainfall at all sites, and pore pressure at some sites in Cascadia

and California. Since installation in 2005, strain signals are observed in the strainmeters related to many geophysical phenomena, including tide (Hodgkinson et al., 2013; Lu & Wen, 2017; Roeloffs, 2010), earthquake (Barbour et al., 2014; Inbal et al., 2017; Roeloffs, 2010), postseismic slip (Alwahedi & Hawthorne, 2019; Hawthorne et al., 2016; Inbal et al., 2017), aseismic creep (Langbein, 2010; Roeloffs, 2010), episodic tremor and slip (Dragert & Wang, 2011; Hawthorne & Rubin, 2010; Kelin Wang et al., 2008), hydrological deformation (Barbour, 2015; Barbour & Wyatt, 2014; Lu & Wen, 2018), and lake seiche (Luttrell et al., 2013).

We download the NOTA borehole strain (level 2) and pore pressure data from UNAVCO. We eliminate data outliers, remove barometric pressure response, tidal signal and borehole trend from the original strain data, and obtain the residual strain signal. We further use the tidal calibration matrixes (Hodgkinson et al., 2013) to convert the residual strain from four-gauge measurements to horizontal strain tensor components, including areal strain $E_A = \varepsilon_{ee} + \varepsilon_{nn}$, differential extension $E_D = \varepsilon_{ee} - \varepsilon_{nn}$ and engineering shear strain $E_S = 2\varepsilon_{en}$, where ε_{ee} and ε_{nn} are east-west and north-south normal strains, respectively, and ε_{en} is east-north shear strain.

Strong postseismic deformation signals (with an amplitude up to 10^{-7}) are observed in the residual strain data recorded near Anza, southern California. These signals start immediately after three local earthquakes (Mw > 4.5) and one remote earthquake (Mw 7.2), and last 40–100 days (Figures 1–2 and S1–S2). The postseismic strains of the four

144 earthquakes exhibit similar behaviors, with the postseismic strain at a same gauge of a
145 strainmeter either consistently increasing or decreasing for all the four earthquakes
146 (Figures 2 and S1–S2). The strain rate is large immediately after the earthquakes and
147 decreases over time, with the decreasing rate varying significantly among different
148 strainmeters (Figure 2). Compared to the coseismic static strains, the postseismic strains
149 exhibit larger amplitudes and different relative amplitudes among different strain
150 components (Figure 2).
151
152 The pore pressure recorded at some of the strainmeters also exhibits significant
153 postseismic changes (10^3–10^4 Pa), with the observations of the four earthquakes
154 exhibiting similar increasing or decreasing trend at a same strainmeter (Figures 1–2 and
155 S1–S2). However, the postseismic pore pressure exhibits different behaviors among
156 different strainmeters (Figure 2). At some strainmeters, pore pressure decreases
157 immediately after the earthquakes. For example, pore pressure at B087 decreases
158 immediately after the 2016 Mw 5.2 earthquake, concurrent with the postseismic strain
159 (Figure 2c). At some other strainmeters, the pore pressure decrease has a time delay of
160 4–10 days relative to the occurrence of the earthquakes. For example, pore pressure
161 remains at background level at B086 for about 8 days after the 2016 Mw 5.2 earthquake
162 before exhibiting a significant decrease (Figures 2b and S3). At the other strainmeters,
163 pore pressure exhibits only small or no postseismic changes (Figures 2e and 2f).
164

3. Physical mechanisms for the postseismic strains

As the four earthquakes exhibit similar postseismic behaviors and the data quality for the 2016 Mw 5.2 earthquake is the best among the four earthquakes (Figure 2), we use the observations of this earthquake as an example to explore physical mechanisms for the postseismic strains.

The observed strong postseismic strains cannot be explained by postseismic viscoelastic relaxation, as the relaxation usually produces postseismic strain smaller in amplitude compared to the coseismic static strain on the timescale of several to tens of days, contrary to the observations (Figure 2). Nor can these observed postseismic strains be explained by the fault slip produced by the aftershocks, because the total coseismic static strains produced by the aftershocks are at orders of 10^{-11}–10^{-10} (Figure S4), about 3 orders of magnitude smaller than the observed postseismic strains. Besides, the strains produced by the aftershocks would exhibit different temporal variations from those observed in the postseismic strains (Figure S4).

The correlation between the observed postseismic strains and the postseismic pore pressure changes suggests that at least some of the postseismic strains are likely hydrological in origin. However, the postseismic strains cannot purely be caused by the postseismic pore pressure changes based on the postseismic observations from strainmeters B086 and B084. Note that the strains start changing immediately after the 2016 Mw 5.2 earthquake at B086, but the pore pressure only starts significantly

187 decreasing with a delay of 8 days (Figures 2b and S3). At B084, the pore pressure
188 change after the 2016 Mw 5.2 earthquake lasts only about 10 days, while the
189 postseismic strain lasts at least 30 days (Figure 2a). These postseismic strains observed
190 immediately after the earthquake without concurrent pore pressure changes suggest that
191 the observed postseismic strains cannot purely be explained by the postseismic pore
192 pressure changes alone, and there should be an additional mechanism that produces the
193 observed postseismic strains.
194
195 We show that the observed strong postseismic strains could be explained by combined
196 effects of the postseismic pore pressure change and an earthquake-triggered aseismic
197 slip on a neighboring fault to the mainshock. We decompose the observed postseismic
198 strains into two parts, with one part related to the pore pressure change and the other
199 part produced by an aseismic slip:
200
$$d_{ij}(t) = f_{ij}P_j(t) + G_{ij}M(t), \quad (1)$$

201 where t is time, d_{ij} postseismic strain observed at the ith component (E_A, E_D or
202 E_S) of the jth strainmeter, P_j observed postseismic pore pressure change, f_{ij}
203 proportional factor of the pressure-induced strain to the pore pressure change, M
204 seismic moment of the aseismic slip, and G_{ij} Green's function of static strain produced
205 by a unit aseismic slip. On the right hand side (RHS) of Equation (1), the first term
206 represents the strain produced by the pore pressure change, with each component of the
207 pressure-induced strain at each strainmeter assumed to be linearly proportional to the
208 postseismic pore pressure change at that strainmeter. The second term represents the

strain produced by the aseismic slip, which is assumed to only occur at a point on the fault plane with a consistent focal mechanism during the aseismic slip period. In Equation (1), $d_{ij}(t)$ and $P_j(t)$ are the observed data, while the other parameters are unknowns that are inverted from the data.

We select $d_{ij}(t)$ and $P_j(t)$ that are used in Equation (1) based on the data quality of each strainmeter. We use the data from B084, B086, B087 and B088 for quantitative constraint of the aseismic slip and pore pressure effect based on Equation (1), as these strainmeters record clear postseismic signals that exhibit a high signal-to-noise ratio. For the other strainmeters that exhibit a lower signal-to-noise ratio (B081, B089, B093 and B946), we only use the data from them as qualitative constraints, i.e., we require that the synthetic postseismic strains produced by the aseismic slip be within the magnitudes of the strain variations observed at these strainmeters. We only use the data recorded in the early 30 days after the earthquake, as the cumulative effects of the background strain variations after 30 days would no longer be small enough to be ignored in the postseismic strain data.

We search all possible aseismic slip point sources along the San Jacinto fault zone with a focal mechanism consistent with the local fault slip, and find a best-fitting solution of G_{ij}, $M(t)$ and f_{ij} to Equation (1) through minimizing the following error function:

$$E = \left\| f_{ij}P_j(t) + G_{ij}M(t) - d_{ij}(t) \right\|^2 + \alpha^2 \|LM(t)\|^2, \quad (2)$$

where $\|\cdot\|$ denotes the L_2 norm. On the RHS, the first term is the misfit between the

synthetic and observed postseismic strains. This term is a summation of the misfits for all strain components (E_A, E_D and E_S) of the strainmeters selected as quantitative constraints (B084, B086, B087 and B088) through 0–30 days after the earthquake. G_{ij} is computed using an elastic half-space Earth model (Okada, 1985) with elastic moduli $\lambda = 37.2$ GPa and $\mu = 36.8$ GPa (Laske et al., 2013). The second term is a regularization term that imposes a temporal smoothness on the aseismic fault slip, with L being the second-order Tikhonov regularization operator and α being a smoothness coefficient that controls the relative importance between the misfit and smoothness terms. The value of α is determined through an L-curve analysis, being 4×10^{-29} $\mathrm{day}^2/\mathrm{dyne} \cdot \mathrm{cm}$ (Figure S5).

The best-fitting aseismic solution corresponds to an aseismic slip at depth of 5 km and located 11 km north and 6 km west to the 2016 Mw 5.2 earthquake, with an equivalent magnitude of Mw 4.9 accumulated in the early 30-day's postseismic period and a focal mechanism of strike/dip/rake = 283°/83°/199° (Figures 3a and 3b). The moment rate of the aseismic slip decreases logarithmically over time after the mainshock and has not reached zero at the 30th postseismic day (Figure 3a). The absolute value of the best-fitting strain-pressure proportional factor ranges between 2–125×10^{-10}/Pa for different strain components of the strainmeters. Overall, the total strains of the inferred solutions of aseismic slip and pore pressure-induced deformation fit the observed strains well for those selected for the quantitative inversion (Figure 3). The principal strains of the synthetic strains accumulated in the early 20-day's postseismic period are consistent

253 with those of the observed residual strains in both orientation and amplitude (Figure
254 3b). With the exceptions for the components that contain noise unrelated to the
255 postseismic deformation (c.f., the sudden strain change of E_S at B088 in the second
256 postseismic day), the synthetic time series of the postseismic strains match the observed
257 time series well (Figures 3c–3e). At B086, the strains observed in the early 8-day's
258 postseismic period are mainly explained by the aseismic slip, as the pore pressure
259 change is small in this time period. Additionally, the synthetic postseismic strains
260 produced by the inferred aseismic slip are also within the magnitudes of the strain
261 variations observed at the other strainmeters that are not used as the quantitative
262 constraints (Figure S6).
263
264 Based on the above modeling results, we propose a mechanism that the mainshock
265 event instantly triggers an aseismic slip in a neighboring fault and alters the
266 hydrological conditions in the region; the change of hydrological condition results in
267 postseismic pore pressure changes and produces poroelastic deformation in the region,
268 while the aseismic slip produces elastic deformation (Figure 4). Such mechanism is
269 consistent with the results of our previous study on hydro-related strain at Anza which
270 shows that underground pore fluid could produce significant poroelastic deformation
271 (Lu & Wen, 2018). For the current earthquakes, additional supporting evidence includes:
272 (1) Observation of the postseismic pore pressure change at the multiple strainmeters
273 suggests a broad distribution of pore pressure change, which could produce poroelastic
274 deformation in a broad region, (2) the significant differences of the postseismic pore

pressure change observed among the strainmeters suggest a significant spatial variation of the pore pressure change, which would further promote the poroelastic deformation, and (3) the persistent pore pressure changes observed after all the four earthquakes suggest that the pore fluid would likely change after every large earthquake at the region and produce persistent poroelastic deformation.

We have made two simplifications in the modeling of the observed postseismic strains. First, we have adopted a point source for the aseismic slip model, while a realistic aseismic slip would likely occur with a finite spatial distribution on the fault plane. In the absence of dense geodetic observations in the region, our choice of the point source model for the aseismic slip is a balance between explaining the observed strain data and avoiding overfitting the limited data set. Despite the point source simplification, the existence of the aseismic slip and the decomposition of the slip-related strain from the hydro-related strain are well resolved by the observed residual strain and pore pressure data. Second, we have assumed that the strain induced by the pore pressure change is proportional to the pore pressure change recorded at the site, while the strain should be related to the spatial and temporal changes of pore pressure in the region. While the lack of detailed 3D observations of pore pressure renders the detailed poroelastic modeling impossible, the inferred quantitative relationships between the pore pressure change and the residual strain should be interpreted with caution. However, we believe the linear relationship between the pressure-induced strain and the postseismic pore pressure change is a good assumption based on the high correlation of the time series

297 between the two observations and the fact that they are recorded at the same sites.

298

299 4. Conclusions

300 Strong months-long changes of strain and pore pressure are observed after three Mw
301 4.5+ local and one Mw 7.2 regional earthquakes during 2010–2017 in the NOTA
302 borehole strainmeters near Anza, southern California. The strain change emerges
303 immediately after the earthquakes and last 40–100 days. The postseismic strains of the
304 four earthquakes exhibit similar behaviors, with the postseismic strain at a same gauge
305 of a strainmeter either consistently increasing or decreasing for all the four earthquakes.
306 Compared to the coseismic strain offsets, the postseismic strains exhibit larger
307 amplitudes (up to 10^{-7}) and different relative amplitudes among different strain
308 components. The postseismic pore pressure exhibits similar increasing or decreasing
309 trend (10^{3}–10^{4} Pa) for the four earthquakes at a same strainmeter, but exhibits different
310 behaviors among different strainmeters, with changing immediately after the
311 earthquakes at some sites and exhibiting a time delay of 4–10 days relative to the
312 occurrence of the earthquakes at the others. The observed postseismic strains can be
313 explained by combined effects of poroelastic deformation due to the pore pressure
314 change and elastic deformation due to an aseismic slip on a neighboring fault. Based
315 on the modeling results, we propose a mechanism that the mainshock event instantly
316 triggers an aseismic slip in a neighboring fault and alters the hydrological conditions in
317 the region; the change of hydrological condition results in postseismic pore pressure

changes and produces poroelastic deformation in the region, while the aseismic slip produces elastic deformation Our study indicates that, in addition to possible aseismic fault slips triggered by an earthquake, pore pressure changes after the earthquake could play an even more important role in producing postseismic deformation.

Acknowledgements

The NOTA borehole strain and pore pressure data were downloaded from UNAVCO (http://www.unavco.org/data/strain-seismic/strain-seismic.html/). The figures in the article were prepared using GMT package (Wessel et al., 2013) and Power Point. This research was supported by the China Postdoctoral Science Foundation under grant 2019TQ0301; the National Natural Science Foundation of China under grants 41874002 and 41674045; the Key Research Program of Frontier Sciences of Chinese Academy of Sciences (QYZDY-SSW-DQC020, CAS); and the Natural Science Foundation of Anhui Province of China.

References

Alwahedi, M. A., & Hawthorne, J. C. (2019). Intermediate-magnitude postseismic slip follows intermediate-magnitude (*M* 4 to 5) earthquakes in California. *Geophysical Research Letters, 46*(7), 3676–3687. doi:10.1029/2018gl081001

Barbour, A. J. (2015). Pore pressure sensitivities to dynamic strains: Observations in active tectonic regions. *Journal of Geophysical Research: Solid Earth, 120*(8), 5863–5883. doi:10.1002/2015JB012201

Barbour, A. J., Agnew, D. C., & Wyatt, F. K. (2014). Coseismic strains on Plate Boundary Observatory borehole strainmeters in Southern California. *Bulletin of the Seismological Society of America, 105*(1), 431–444. doi:10.1785/0120140199

Barbour, A. J., & Wyatt, F. K. (2014). Modeling strain and pore pressure associated with fluid extraction: The Pathfinder Ranch experiment. *Journal of Geophysical Research: Solid Earth, 119*(6), 5254–5273. doi:10.1002/2014JB011169

Byerlee, J. (1993). Model for episodic flow of high-pressure water in fault zones before earthquakes. *Geology, 21*(4), 303–306. doi:10.1130/0091-7613(1993)021<0303:mfefoh>2.3.co;2

Dragert, H., & Wang, K. (2011). Temporal evolution of an episodic tremor and slip event along the northern Cascadia margin. *Journal of Geophysical Research, 116*(B12), B12406. doi:10.1029/2011JB008609

Fu, Y., & Freymueller, J. T. (2012). Seasonal and long-term vertical deformation in the Nepal Himalaya constrained by GPS and GRACE measurements. *Journal of Geophysical Research, 117*(B3), B03407. doi:10.1029/2011JB008925

Gladwin, M. T. (1984). High-precision multicomponent borehole deformation monitoring. *Review of Scientific Instruments, 55*(12), 2011–2016. doi:10.1063/1.1137704

Gualandi, A., Liu, Z., & Rollins, C. (2020). Post-large earthquake seismic activities mediated by aseismic deformation processes. *Earth and Planetary Science Letters, 530*, 115870. doi:10.1016/j.epsl.2019.115870

Hamling, I. J., & Upton, P. (2018). Observations of aseismic slip driven by fluid pressure following the 2016 Kaikōura, New Zealand, earthquake. *Geophysical Research Letters, 45*(20), 11030–11039. doi:10.1029/2018GL079224

Hawthorne, J. C., & Rubin, A. M. (2010). Tidal modulation of slow slip in Cascadia. *Journal of Geophysical Research, 115*(B9), B09406. doi:10.1029/2010jb007502

Hawthorne, J. C., Simons, M., & Ampuero, J. P. (2016). Estimates of aseismic slip associated with small earthquakes near San Juan Bautista, CA. *Journal of Geophysical Research: Solid Earth, 121*(11), 8254–8275. doi:10.1002/2016jb013120

Helmstetter, A., & Shaw, B. E. (2009). Afterslip and aftershocks in the rate-and-state friction law. *Journal of Geophysical Research, 114*(B1), B01308. doi:10.1029/2007jb005077

Hodgkinson, K., Langbein, J., Henderson, B., Mencin, D., & Borsa, A. (2013). Tidal calibration of plate boundary observatory borehole strainmeters. *Journal of Geophysical Research: Solid Earth, 118*(1), 447–458. doi:10.1029/2012JB009651

380 Hu, Y., Bürgmann, R., Banerjee, P., Feng, L., Hill, E. M., Ito, T., . . . Wang, K. (2016).
381 Asthenosphere rheology inferred from observations of the 2012 Indian Ocean
382 earthquake. *Nature, 538*(7625), 368–372. doi:10.1038/nature19787
383 Hughes, K. L. H., Masterlark, T., & Mooney, W. D. (2010). Poroelastic stress-triggering
384 of the 2005 M8.7 Nias earthquake by the 2004 M9.2 Sumatra–Andaman
385 earthquake. *Earth and Planetary Science Letters, 293*(3–4), 289–299.
386 doi:10.1016/j.epsl.2010.02.043
387 Iinuma, T., Hino, R., Uchida, N., Nakamura, W., Kido, M., Osada, Y., & Miura, S.
388 (2016). Seafloor observations indicate spatial separation of coseismic and
389 postseismic slips in the 2011 Tohoku earthquake. *Nature Communications, 7*,
390 13506. doi:10.1038/ncomms13506
391 Inbal, A., Ampuero, J.-P., & Avouac, J.-P. (2017). Locally and remotely triggered
392 aseismic slip on the central San Jacinto Fault near Anza, CA, from joint inversion
393 of seismicity and strainmeter data. *Journal of Geophysical Research: Solid Earth,*
394 *122*(4), 3033–3061. doi:10.1002/2016jb013499
395 Johanson, I. A., Fielding, E. J., Rolandone, F., & Bürgmann, R. (2006). Coseismic and
396 postseismic slip of the 2004 Parkfield earthquake from space-geodetic data.
397 *Bulletin of the Seismological Society of America, 96*(4B), S269–S282.
398 doi:10.1785/0120050818
399 Johnson, K. M., Johnson, K. M., Bürgmann, R., & Larson, K. (2006). Frictional
400 properties on the San Andreas fault near Parkfield, California, inferred from
401 models of afterslip following the 2004 earthquake. *Bulletin of the Seismological*

Society of America, 96(4B), S321–S338. doi:10.1785/0120050808

Jónsson, S. (2008). Importance of post-seismic viscous relaxation in southern Iceland. *Nature Geoscience, 1*(2), 136–139. doi:10.1038/ngeo105

Jónsson, S., Segall, P., Pedersen, R., & Björnsson, G. (2003). Post-earthquake ground movements correlated to pore-pressure transients. *Nature, 424*(6945), 179–183. doi:10.1038/nature01776

Langbein, J. (2010). Effect of error in theoretical Earth tide on calibration of borehole strainmeters. *Geophysical Research Letters, 37*(21), L21303. doi:10.1029/2010GL044454

Laske, G., Masters., G., Ma, Z., & Pasyanos, M. (2013). *Update on CRUST1.0 - A 1-degree global model of Earth's crust.* Paper presented at the EGU.

Lu, Z., & Wen, L. (2017). Abnormally strong daily-cycle S_1 strain tide: Observation and physical mechanism. *Journal of Geophysical Research: Solid Earth, 122*(10), 8525–8537. doi:10.1002/2017JB014383

Lu, Z., & Wen, L. (2018). Strong hydro‐related localized long‐period crustal deformation observed in the Plate Boundary Observatory borehole strainmeters. *Geophysical Research Letters, 45*(23), 12856–12865. doi:10.1029/2018gl080856

Luttrell, K., Mencin, D., Francis, O., & Hurwitz, S. (2013). Constraints on the upper crustal magma reservoir beneath Yellowstone Caldera inferred from lake-seiche induced strain observations. *Geophysical Research Letters, 40*(3), 501–506. doi:10.1002/grl.50155

424 Manga, M., & Wang, C.-Y. (2007). Earthquake hydrology. In H. Kanamori & G.
425 Schubert (Eds.), *Treatise on Geophysics* (Vol. 4, pp. 293–320). Amsterdam:
426 Elsevier.
427 Matsumoto, N., Kitagawa, G., & Roeloffs, E. A. (2003). Hydrological response to
428 earthquakes in the Haibara well, central Japan - I. Groundwater level changes
429 revealed using state space decomposition of atmospheric pressure, rainfall and
430 tidal responses. *Geophysical Journal International, 155*(3), 885–898.
431 doi:10.1111/j.1365-246X.2003.02103.x
432 Nur, A., & Mavko, G. (1974). Postseismic viscoelastic rebound. *Science, 183*(4121),
433 204–206. doi:10.1126/science.183.4121.204
434 Okada, Y. (1985). Surface deformation due to shear and tensile faults in a half-space.
435 *Bulletin of the Seismological Society of America, 75*(4), 1135–1154.
436 Peltzer, G., Rosen, P., Rogez, F., & Hudnut, K. (1998). Poroelastic rebound along the
437 Landers 1992 earthquake surface rupture. *Journal of Geophysical Research,*
438 *103*(B12), 30131–30145. doi:10.1029/98jb02302
439 Roeloffs, E. A. (1998). Persistent water level changes in a well near Parkfield,
440 California, due to local and distant earthquakes. *Journal of Geophysical Research,*
441 *103*(B1), 869–889. doi:10.1029/97jb02335
442 Roeloffs, E. A. (2010). Tidal calibration of Plate Boundary Observatory borehole
443 strainmeters: Roles of vertical and shear coupling. *Journal of Geophysical*
444 *Research, 115*, B06405. doi:10.1029/2009JB006407
445 Ross, Z. E., Kanamori, H., & Hauksson, E. (2017). Anomalously large complete stress

446 drop during the 2016 Mw 5.2 Borrego Springs earthquake inferred by waveform
447 modeling and near-source aftershock deficit. *Geophysical Research Letters,*
448 *44*(12), 5994–6001. doi:10.1002/2017gl073338
449 Scholz, C. H., Wyss, M., & Smith, S. W. (1969). Seismic and aseismic slip on the San
450 Andreas fault. *Journal of Geophysical Research, 74*(8), 2049–2069.
451 doi:10.1029/JB074i008p02049
452 Sibson, R. H. (1992). Implications of fault-valve behaviour for rupture nucleation and
453 recurrence. *Tectonophysics, 211*(1–4), 283–293. doi:10.1016/0040-
454 1951(92)90065-e
455 Silver, P. G., & PBO Steering Committee. (2000). The Plate Boundary Observatory
456 white paper: Creating a four-D image of the deformation of western North
457 America.
458 Silverii, F., D'Agostino, N., Borsa, A. A., Calcaterra, S., Gambino, P., Giuliani, R., &
459 Mattone, M. (2019). Transient crustal deformation from karst aquifers hydrology
460 in the Apennines (Italy). *Earth and Planetary Science Letters, 506*, 23–37.
461 doi:10.1016/j.epsl.2018.10.019
462 Smith, S. W., & Wyss, M. (1968). Displacement on the San Andreas fault subsequent
463 to the 1966 Parkfield earthquake. *Bulletin of the Seismological Society of America,*
464 *58*(6), 1955–1973.
465 Wang, C.-Y., & Barbour, A. J. (2017). Influence of pore pressure change on coseismic
466 volumetric strain. *Earth and Planetary Science Letters, 475*, 152–159.
467 doi:10.1016/j.epsl.2017.07.034

468 Wang, C.-Y., Wang, C.-H., & Manga, M. (2004). Coseismic release of water from
469 mountains: Evidence from the 1999 (Mw = 7.5) Chi-Chi, Taiwan, earthquake.
470 *Geology, 32*(9), 769–772. doi:10.1130/g20753.1
471 Wang, K., Dragert, H., Kao, H., & Roeloffs, E. (2008). Characterizing an
472 "uncharacteristic" ETS event in northern Cascadia. *Geophysical Research Letters,*
473 *35*(15), L15303. doi:10.1029/2008GL034415
474 Wang, K., & Fialko, Y. (2018). Observations and modeling of coseismic and
475 postseismic deformation due to the 2015 Mw 7.8 Gorkha (Nepal) earthquake.
476 *Journal of Geophysical Research: Solid Earth, 123*(1), 761–779.
477 doi:10.1002/2017jb014620
478 Wessel, P., Smith, W. H. F., Scharroo, R., Luis, J., & Wobbe, F. (2013). Generic
479 Mapping Tools: Improved version released. *Eos, Transactions American*
480 *Geophysical Union, 94*(45), 409–410. doi:10.1002/2013EO450001
481 Xu, X., Sandwell, D. T., Ward, L. A., Milliner, C. W. D., Smith-Konter, B. R., Fang, P.,
482 & Bock, Y. (2020). Surface deformation associated with fractures near the 2019
483 Ridgecrest earthquake sequence. *Science, 370*(6516), 605–608.
484 doi:10.1126/science.abd1690
485 Yu, S.-B., Hsu, Y.-J., Kuo, L.-C., & Chen, H.-Y. (2003). GPS measurement of
486 postseismic deformation following the 1999 Chi-Chi, Taiwan, earthquake.
487 *Journal of Geophysical Research, 108*(B11), 2520. doi:10.1029/2003jb002396
488 Zhan, W., Li, F., Hao, W., & Yan, J. (2017). Regional characteristics and influencing
489 factors of seasonal vertical crustal motions in Yunnan, China. *Geophysical*

Journal International, 210(3), 1295–1304. doi:10.1093/gji/ggx246

Figures and captions

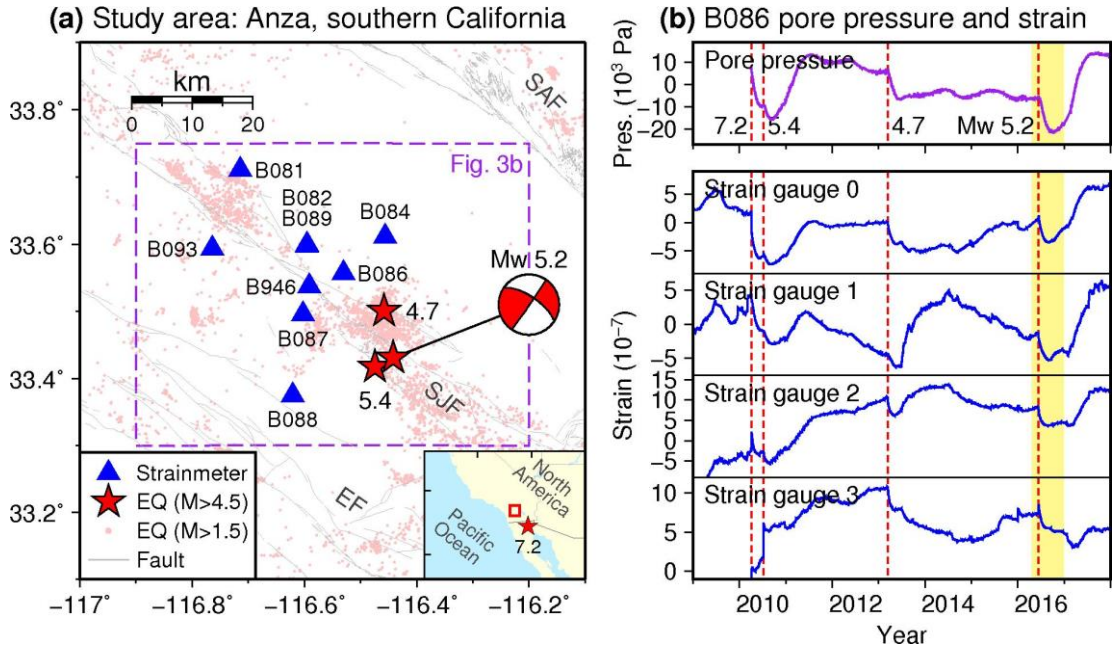

Figure 1. Study area and an example observation of pore pressure and strain from strainmeter B086. (a) Study area showing NOTA strainmeters (blue triangles), earthquakes (red stars and pink points for magnitudes larger than 4.5 and 1.5, respectively) and faults (grey lines) near Anza, southern California, with the strainmeter names, earthquake magnitudes and fault names (SAF: San Andreas fault. SJF: San Jacinto fault. EF: Elsinore fault) labeled. The beach ball represents the focal mechanism (strike/dip/rake = 304°/68°/179°) of the 10 June 2016 Borrego Springs Mw 5.2 earthquake (Ross et al., 2017). The inset shows the map region of Figure 1a within North America (red box) and the location of a regional Mw 7.2 earthquake (red star). **(b)** Pore pressure (purple curve) and strain (blue curves) observed during 2009–2017 at strainmeter B086, with the occurrence time of the four Mw 4.5+ earthquakes marked with vertical dashed lines (with magnitudes labeled beside). The shaded yellow bar highlights the 2016 Mw 5.2 earthquake shown in Figure 2. Note the significant changes

of pore pressure and strain after each Mw 4.5+ earthquake.

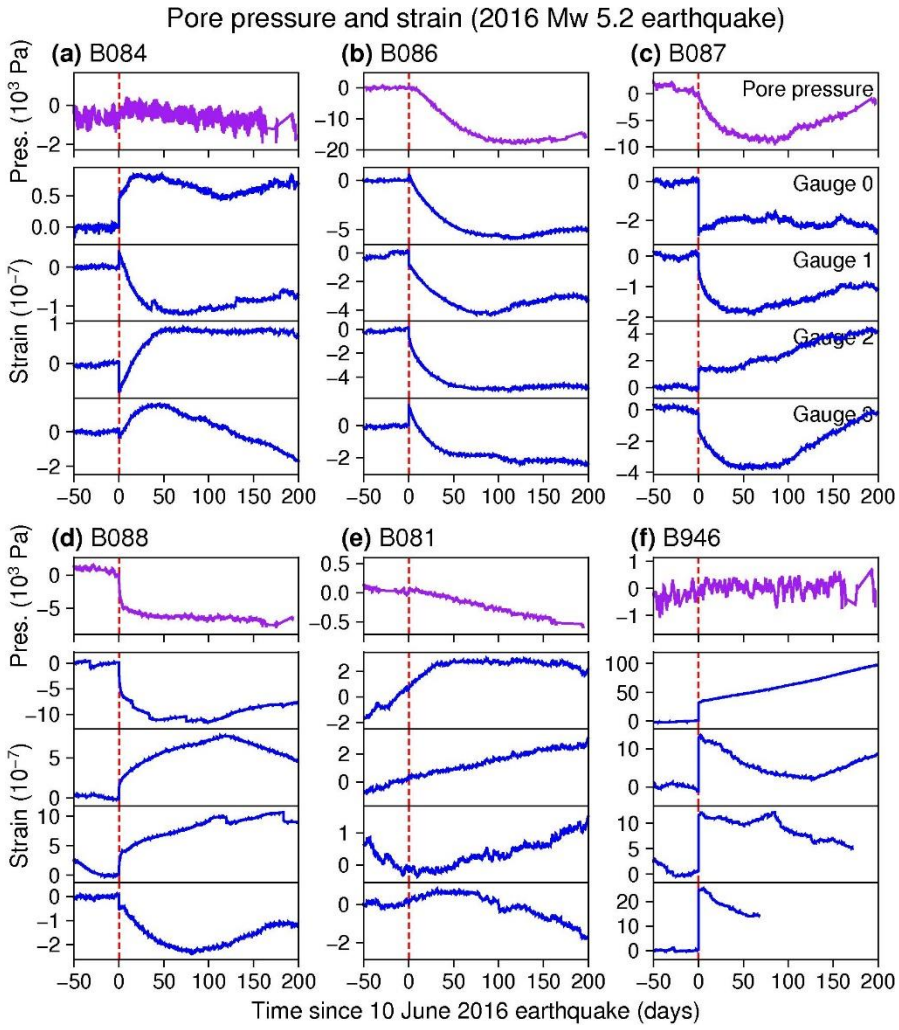

Figure 2. Pore pressure (purple curves) and strain (blue curves) before and after the 2016 Mw 5.2 earthquake observed at strainmeters B084, B086, B087, B088, B081 and B946. Each strain component has been removed a linear trend before the earthquake. The vertical dashed line in each panel marks the occurrence time of the earthquake. Data containing large noise has been removed from gauges 2 and 3 of B946.

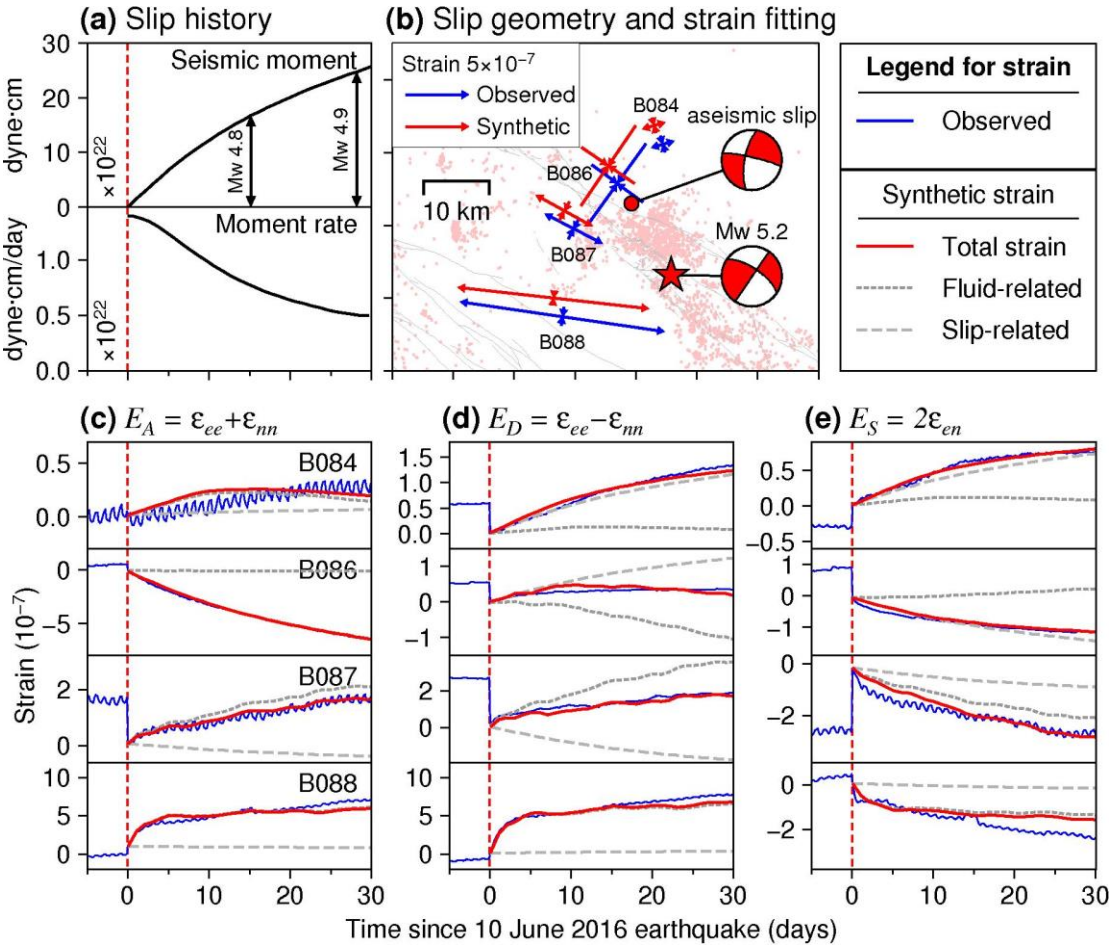

519

520 **Figure 3. The best-fitting postseismic aseismic slip and comparison between the**
521 **observed and synthetic postseismic strains. (a)** Seismic moment and moment rate of
522 the best-fitting aseismic slip as a function of time. **(b)** Location and focal mechanism
523 of the best-fitting aseismic slip, and a comparison between the observed and synthetic
524 postseismic strains (blue and red crosses, respectively) accumulated in the early 20 days
525 after the 2016 earthquake. The direction and length of the crosses represent orientation
526 and magnitude of the principal strains, with the vectors pointing outward (inward)
527 representing elongation (compression) in that orientation. Locations of the synthetic
528 strains are plotted offset for clarity. **(c–e)** Time series of the observed (blue solid curves)
529 and synthetic strains (red solid, grey short-dashed and grey long-dashed curves for the
530 total, fluid-related and slip-related strains, respectively) for (c) areal strain E_A, (d)

differential extension E_D, and (e) engineering shear strain E_S.

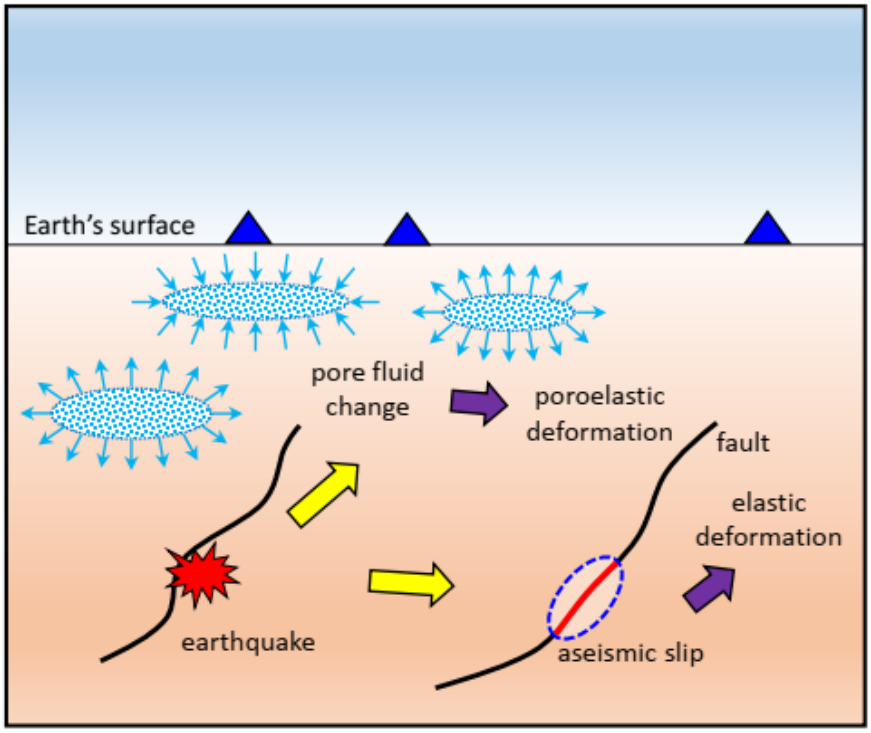

Figure 4. Cartoon illustrating the physical mechanism in which an earthquake triggers both pore fluid change and an aseismic slip, which subsequently produce postseismic deformation. The mainshock earthquake instantly triggers an aseismic slip in a neighboring fault and alters the hydrological conditions in the region; the change of hydrological condition results in postseismic pore pressure changes and produces poroelastic deformation in the region, while the aseismic slip produces elastic deformation.